http://journal.uir.ac.id/index.php/JGEET

E-ISSN : 2541-5794
P-ISSN : 2503-216X

Journal of Geoscience,
Engineering, Environment, and Technology
Vol 11 No 3 2025

RESEARCH ARTICLE

# Numerical Analysis of Joint-Controlled Slope Stability under Blasting-Induced Vibration: A Case Study of the Jakarta-Bandung High-Speed Railway Tunnel 4

Fariz Aditya [1,*], Budi Sulistianto [2] , Tri Karian [2], Simon Heru Prassetyo [2] , Ganda Marihot Simangunsong [2]

[1] *Mining Engineering Department, Universitas Negeri Padang, Indonesia.*
[2] *Mining Engineering Study Program, Institut Teknologi Bandung, Indonesia.*

* Corresponding author : farizaditya@unp.ac.id
Tel.:+6281363104085
Received: Jul 30, 2026; Accepted: Sep 17, 2026.
DOI: 10.24273/jgeet.2016.1.2.001

**Abstract**

Blasting for Tunnel 4 of the Jakarta–Bandung High-Speed Railway is conducted close to an active andesite quarry, where blast-induced vibration may interact with pre-existing discontinuities and groundwater to reduce slope stability. This study evaluates the combined effects of joint structure, groundwater conditions, and tunnel-blasting vibration on quarry-slope stability using two-dimensional finite-element analysis in RS2 with the shear-strength-reduction method. Field characterization comprised scanline discontinuity mapping, rock-mass classification, laboratory testing, and Minimate vibration monitoring. Jointless and explicitly jointed slope models were evaluated under four scenarios: dry-static, dry-dynamic, saturated-static, and saturated-dynamic. The monitored blast dataset was additionally evaluated using the site-specific scaled-distance relationship, $PPV = 156.3(SD)^{-1.056}$ ($R^2=0.376$), where $SD = R/\sqrt{Q}$, to characterize vibration attenuation and its uncertainty. Under static conditions, explicit joints reduced the factor of safety (FoS) by 3% in the dry model and 6% in the saturated model. Under dynamic conditions, the joint-related FoS reduction increased to 15% in the dry model (4.1 to 3.5) and 42% in the saturated model (3.4 to 2.0), with the probability of failure reaching 17% in the critical saturated-dynamic-jointed scenario. A charge-per-delay sensitivity analysis at a fixed source-to-slope distance of 25 m further showed that increasing explosive charge progressively increased the predicted longitudinal peak particle acceleration (PPA) and reduced slope stability. Based on the adopted stability criteria, the analysis supports maximum site-specific charges of 30 kg/delay under dry conditions and 20 kg/delay under saturated conditions at 25 m. These results demonstrate that groundwater saturation substantially amplifies the destabilizing influence of blasting on joint-controlled slope response and highlight the need for groundwater-dependent blast control, controlled trial blasts, and field monitoring before operational implementation.

**Keywords:** landslide, slope stability, blasting vibration, tunnel excavation, mitigation



## 1. Introduction

Slope stability is a fundamental geotechnical requirement in open-pit mining because instability can cause production losses, equipment damage, injuries, and fatalities. The stability of a rock slope is governed by slope geometry, rock-mass strength, groundwater pressure, and the orientation and persistence of discontinuities. Recent studies have emphasized the need to integrate geological structure and groundwater conditions rather than treating the slope as a homogeneous continuum (Du et al., 2022; Sun et al., 2024; Putra et al., 2026). Excavation of slope stability in open-pit mining in the mining industry is one of the important issues, as it relates to the increase in production of mining companies in Indonesia. As a result, these mining companies are expanding and deepening their excavations. The wider and deeper the open-pit mine is excavated, the greater the risks that will arise or the more uncertainty will increase regarding the factors affecting the stability of the open-pit slope (Azizi, 2018; Aditya et al., 2025).

Discontinuities can provide preferential shear surfaces and therefore alter both the magnitude of the factor of safety and the governing failure mechanism. Their influence becomes particularly important when transient loading is superimposed on the static stress state. For jointed rock, shear resistance depends on effective normal stress, joint roughness, joint-wall strength, and persistence The open-pit mine's high slope differs compared to the usual mine slope landslide mechanism. Given the high stress and powerful unloading effect caused by the open-pit mine's high slope, landslide accidents are going to occur during the excavation and unloading process, which increases the likelihood of landslides and mining difficulties (Devy and Hutahayan, 2021; Wang et al., 2023).

Blasting introduces short-duration stress waves and ground vibration that may trigger additional displacement or mobilize pre-existing discontinuities (Irwandy Arif, 2016). Peak particle velocity (PPV), peak particle acceleration (PPA), charge weight per delay, and source-to-monitor distance are commonly used to characterize blast vibration (Prassetyo et al., 2024). Previous studies have developed empirical and data-driven relationships for predicting blast-induced vibration and assessing its effect on slopes and nearby infrastructure (Ma et al., 2021; Sun and Li, 2023).

Despite this progress, many slope-blasting studies evaluate vibration, groundwater, or discontinuity effects separately. Fewer studies explicitly compare jointless and jointed numerical models under a common matrix of dry/saturated and static/dynamic conditions while also linking monitored tunnel-blast vibration to operational blast-control recommendations (Wang et al., 2023). This combined vibration-joint-water interaction is especially relevant where underground tunnel blasting occurs immediately adjacent to an active quarry slope (Lee et al., 2013; Luo et al., 2023). The present study addresses this gap by explicitly representing the mapped critical joint set in a finite-element slope model and comparing its response with an equivalent jointless model (Jiang F., Xiong, Y., Han, R., 2014; Xiong et al., 2021).

The study site is an andesite quarry in Sukajaya Village, Sukatani District, Purwakarta Regency, adjacent to Tunnel 4 of the Jakarta-Bandung High-Speed Railway. Tunnel excavation employed drilling and blasting, whereas the nearby quarry used mechanical excavation. Consequently, the vibration source evaluated in this study is the tunnel blast, not quarry blasting. The proximity of the tunnel alignment to the existing quarry slope provides a field setting in which blast-induced loading, discontinuity geometry, and groundwater condition can interact (Ma et al., 2025; Heriyadi et al., 2026).

Accordingly, this study aims to: (1) characterize the rock mass and discontinuities of the critical quarry slope; (2) quantify the attenuation of monitored tunnel-blast vibration using scaled distance; (3) evaluate slope stability using RS2 under dry-static, dry-dynamic, saturated-static, and saturated-dynamic conditions; (4) quantify the incremental effect of explicitly modeled joints on FoS, probability of failure, and failure mechanism; and (5) assess site-specific blast-control implications at the minimum source-to-slope distance. The novelty of the study lies in the integrated comparison of joint structure, groundwater saturation, and blast-induced loading within the same numerical scenario matrix.

## 2. Materials and Methodology

### 2.1 Mining Area around the Tunnel

The study area is located in Sukatani District, Purwakarta Regency, West Java, Indonesia, within approximately 765,600–767,100 m E and 9,269,900–9,271,300 m N in the WGS 1984/UTM Zone 48S coordinate system. Tunnel 4 follows a southwest–northeast alignment and passes through the quarry area, where the analyzed slope is located adjacent to the tunnel alignment (Fig. 1). The spatial configuration of the tunnel, quarry workings, and surrounding terrain was established from the January 2020 aerial photograph and site mapping.

The andesite quarry itself was excavated mechanically using rock breakers and hand tools; therefore, the monitored vibration reported in this study originates from tunnel blasting. Figure 2 illustrates the quarry condition and the exposed rock slope near the tunnel corridor.

### 2.2 Rock Mass Characterization

Rock-mass characterization was performed through direct engineering-geological mapping and systematic scanline discontinuity mapping on accessible quarry faces (Figures 3 and 4). The scanline mapping was conducted along an approximately 60-m-long rock exposure and subdivided into 1-m observation intervals, resulting in 60 measurement segments. For each interval, the recorded parameters included intact rock strength class, Rock Quality Designation (RQD), discontinuity spacing, persistence, aperture or separation, surface roughness, infilling material, weathering condition, groundwater condition, and discontinuity orientation. These field data were used to determine the basic Rock Mass Rating (RMR) and to characterize the discontinuities considered in the numerical slope model.

The scanline data indicate that discontinuity spacing predominantly ranges from 6–20 cm to 20–60 cm, while persistence is mainly within 1–3 m, with locally shorter (<1 m) and longer (3–10 m) discontinuities. Apertures are generally small, predominantly between 0.1 and 1 mm, and the discontinuity surfaces are classified as slightly rough to rough. The mapped rock mass ranges from slightly to moderately weathered, with localized highly weathered zones, and wet groundwater conditions were recorded along the mapped exposure. The calculated RQD values average approximately 86.9%, indicating generally good rock-mass quality. Discontinuity-orientation measurements were subsequently used to identify the dominant joint sets and to select the representative discontinuity incorporated explicitly into the numerical model.

Based on the RMR assessment summarized in Table 1, the investigated rock mass has a basic RMR value of 62. This value was obtained from the individual ratings for intact rock strength, RQD, discontinuity spacing, discontinuity condition, and groundwater condition. The resulting RMR indicates the overall engineering quality of the rock mass and, together with the mapped discontinuity characteristics, provides the geotechnical basis for the subsequent numerical slope-stability analysis.

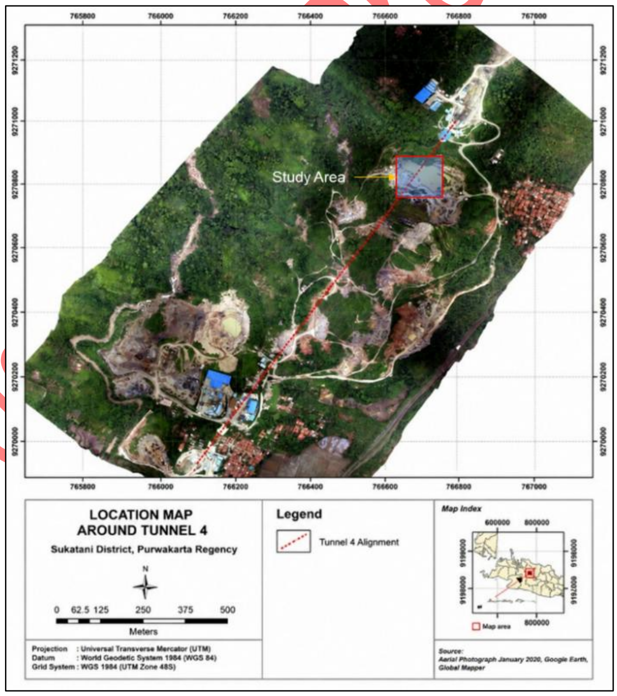


Fig. 1. Location of Tunnel 4

### 2.3 Rock Mass Properties

Soil and rock samples obtained from geotechnical drilling and field sampling were subjected to laboratory testing to characterize the physical and mechanical properties of the identified geotechnical units.

Fig. 2. Quarry Mines Around The Tunnel

Fig. 3. Determination of rock mass characteristics directly in the field

Fig. 4. Geotechnical mapping using the scanline method.

Table 1. Rock Mass Rating (RMR) parameters.

| Parameter | Fresh Andesite Description | Rating |
|---|---|---|
| Uniaxial Compressive Strength | 50–100 MPa | 7 |
| Rock Quality Designation | 90–100 % | 20 |
| Spacing of Discontinuity | 0.6–2 m | 15 |
| Condition of discontinuity | | |
| Length, persistence | > 20 m | 0 |
| Separation | > 5 mm | 0 |
| Roughness | Slightly rough | 3 |
| Infilling | > 5 mm | 2 |
| Weathering | Slightly weathered | 5 |
| Subtotal | | 10 |
| General Cond. of Groundwater | Damp | 10 |
| Total RMR | | 62 |

Physical-properties tests were conducted to determine rock density, while Uniaxial Compressive Strength (UCS) tests were performed on intact rock specimens to determine the intact compressive strength ($\sigma_c$). The UCS testing system was instrumented to record both axial and lateral strains, allowing Young's modulus (E) and Poisson's ratio (ν) to be determined from the measured stress–strain response. Direct shear tests were also conducted to determine the shear-strength parameters, namely cohesion (c) and friction angle (ϕ).

The laboratory test results represent the physical and mechanical properties of the tested intact rock specimens. These laboratory-derived properties, together with the rock-mass characterization described in Section 2.2, were used to establish representative rock-mass parameters for the geotechnical units considered in the site characterization. The resulting parameters, including rock-mass compressive strength (σcm), rock-mass deformation modulus (Erm), Poisson's ratio (νm), rock-mass cohesion (cm), and rock-mass friction angle (ϕm), are summarized in Table 2.

Although Table 2 presents the parameters for all geotechnical units identified across the study area, the critical numerical cross-section analyzed in RS2 is dominated by slightly weathered to fresh andesite (SW/F-An). Consequently, only the representative parameter set for this unit was assigned to the modeled slope domain. For transparency and reproducibility, the parameters adopted in the RS2 model are reproduced separately in Table 4. The remaining geotechnical units listed in Table 2 represent the broader site characterization and are not intersected by the critical cross-section considered in the present numerical analysis.

### 2.4 Joint Properties

Discontinuity properties were used to represent the reduction in shear resistance along pre-existing joint planes. The numerical interface parameters comprise joint-wall compressive strength (JCS), joint roughness coefficient (JRC), normal stiffness (Kn), and shear stiffness (Ks) (Al Mandalawi, 2024; Al-E'Bayat et al., 2024). The critical joint set was selected from the scanline dataset according to its orientation relative to the slope face and its persistence. Joint shear behavior was represented using a Mohr-Coulomb slip criterion, while Kn and Ks were calculated from the stiffness relationships shown in Eqs. (1) and (2) (Barton, 1972). This explicit-joint representation allows the model to distinguish structurally controlled deformation from failure through the equivalent rock mass.

$$Kn = \frac{Ei\ Em}{L(Ei-Em)} \quad (1)$$

Em = modulus of rock mass
Ei = modulus of intact rock
L = mean spacing of joint

$$Ks = \frac{Gi\ Gm}{L(Gi-Gm)} \quad (2)$$

Gm = Shear modulus of rock mass
Gi = Shear modulus of intact rock
L = mean spacing of joint

### 2.5 Blast Vibration Monitoring and Attenuation

Tunnel-blast vibration was monitored using three Minimate units: two around the quarry and one near the residential area. Monitoring points at the quarry were positioned near the slope toe. For each blast event, the instrument recorded PPV components in the transverse, vertical, and longitudinal directions, together with peak vector sum (PVS). The dataset also contains source-to-monitor distance (R) and maximum explosive charge per delay (Qmax). Table 3 summarizes the 11 monitored tunnel-blast events collected during June-July 2020.

Besides the vibration amplitude, each measurement is also associated with the distance from the blast point to the monitoring point (R), the maximum charge weight per delay (Qmax), and the resulting scaled distance (SD), which is calculated as SD = R/√Qmax. The scaled distance concept is commonly used in blast vibration studies because it

Scaled distance was calculated using the square-root scaling relationship SD = R/sqrt(Qmax), where R is in metres and Qmax is in kilograms per delay. A log-log least-squares regression of the maximum component PPV against SD for the 11 events gives the site-specific attenuation equation PPV = 156.3(SD)^-1.056, with $R^2$ = 0.376. At the 25 m design distance, the regression predicts PPV values of approximately 25.4 mm/s for 20 kg/delay and 31.4 mm/s for 30 kg/delay. The relatively low $R^2$ indicates substantial event-to-event scatter; therefore, the regression is used as an attenuation screening relationship rather than as a stand-alone deterministic safety criterion (Dowding, 1985; Zvarivadza et al., 2025).

The monitored PPV values range from approximately 1 to 27 mm/s, reflecting variations in charge weight, propagation distance, local geology, and blast configuration. The July 9, 2020 event was retained as the representative dynamic event because the available dataset includes corresponding PPA components (Table 5). PPV and PPA are treated as distinct measured vibration descriptors; no direct PPV-to-PPA conversion is assumed in the revised manuscript.

The recorded vibration data, summarized in Table 3, shows considerable variation in PPV values, ranging from about 1 mm/s up to more than 27 mm/s, depending on the charge weight used and the distance between the blast point and the monitoring location. This dataset serves two purposes in this study: first, to characterize the attenuation trend of blast-induced vibration around the quarry area, and second, to provide the basis for selecting the representative Peak Particle Acceleration (PPA) value used as the dynamic loading input in the slope stability model, as discussed in Section 3.1.

### 2.6 Numerical Model and Scenario Definition

The critical quarry slope was analyzed using the two-dimensional finite-element program RS2. Slope stability was evaluated using shear-strength reduction (SSR), in which cohesion and frictional resistance are progressively reduced until numerical non-convergence or a continuous failure mechanism develops; the corresponding strength-reduction factor is reported as the factor of safety (FoS). The modeled material is slightly weathered to fresh andesite with the rock-mass parameters in Table 4.

The two-dimensional numerical model was constructed using the actual topographic profile of the critical quarry cross-section obtained from the field topographic survey. The model domain was extended beyond the slope crest and toe to minimize potential boundary effects. The ground surface was maintained as a free boundary, while the left and right lateral boundaries were restrained against horizontal displacement and allowed to move vertically. The basal boundary was restrained in both the horizontal and vertical directions. The model domain was discretized using a graded triangular finite-element mesh conforming to the irregular slope geometry, with local refinement applied along the slope surface and discontinuity interfaces. An SSR search area was defined around the critical slope to focus the identification of the potential failure mechanism within the geotechnically relevant slope domain. The same model geometry, mesh strategy, boundary conditions, and SSR search area were maintained throughout the scenario analyses so that differences in the calculated FoS could be attributed specifically to variations in joint configuration, groundwater condition, and blasting-induced loading rather than to changes in numerical configuration (Gofar and Rahardjo, 2017).

For each SSR calculation, a common strength-reduction factor was progressively applied to the shear-strength parameters until the critical state was reached. The strength-reduction factor corresponding to failure is reported consistently as the factor of safety (FoS) throughout this study (Wong, H. N. dan Pang, 1992). Probability of failure (PoF) values are reported from the probabilistic RS2 analysis to complement the deterministic FoS results and to provide an additional measure of the likelihood of slope instability under the investigated scenarios (Ma et al., 2021).

The dynamic scenarios were represented using a pseudo-static approach based on the measured Peak Particle Acceleration (PPA) data presented in Table 5. The July 9, 2020 vibration record yielded transverse, vertical, and longitudinal PPA values of 0.374g, 0.684g, and 0.529g, respectively. Among the measured vibration components, the longitudinal PPA was adopted as the governing dynamic input because sensitivity evaluation of the slope model indicated that this component produced the greatest influence on slope stability. Accordingly, the longitudinal PPA of 0.529g was applied as the pseudo-static acceleration input in the RS2 model. Because the measured acceleration is expressed relative to gravitational acceleration, the corresponding dimensionless pseudo-static coefficient is defined as $k=a/g$, resulting in a coefficient of $k=0.529$ for the adopted longitudinal component. The same dynamic-loading condition was maintained in the jointless and jointed models and under the corresponding groundwater scenarios to enable direct comparison of the blasting-induced effects on FoS.



Table 2. Rock Mass Strength Parameter

| No. | Lithology | Symbol | $\rho$ (kg/m3) | $\sigma_{cm}$ (MPa) | Erm (MPa) | $v_m$ | $c_m$ (MPa) | $\Phi_m$ (°) |
|---|---|---|---|---|---|---|---|---|
| 1 | Tallus deposits | Td | 1700 | 0.15 | 306 | 0.30 | 0.06 | 15 |
| 2 | Completely weathered soil-volcanic | S-v | 1800 | 0.20 | 314 | 0.30 | 0.08 | 14 |
| 3 | Highly weathered volcanic | HW-v | 2000 | 2.70 | 909 | 0.31 | 0.13 | 18 |
| 4 | Completely weathered Andesite | S-An | 1800 | 0.30 | 331 | 0.30 | 0.12 | 14 |
| 5 | Moderately weathered andesite | MW-An | 2400 | 2.70 | 909 | 0.31 | 0.40 | 27 |
| 6 | Slightly weathered and/or fresh andesite | SW/F-An | 2600 | 13.00 | 2010 | 0.29 | 1.60 | 40 |
| 7 | Completely weathered soil-mudstone | S-Ms | 1800 | 0.30 | 331 | 0.30 | 0.12 | 13 |
| 8 | Moderately weathered mudstone | MW-Ms | 2100 | 0.70 | 399 | 0.30 | 0.27 | 15 |
| 9 | Slightly weathered and/or fresh mudstone | SW/F-Ms | 2100 | 0.80 | 416 | 0.30 | 0.30 | 17 |

Table 3. Vibration Measurement Data

| No | Day/Date | Distance, R (m) | Qmax (kg) | SD (m/kg^1/2) | PPV (mm/s) Tran | Vert | Long | PVS (mm/s) | $PPV_{max}$ (mm/s) |
|---|---|---|---|---|---|---|---|---|---|
| 1 | Monday, 22 June 2020 | 105.2 | 36.8 | 17 | 5.18 | 4.91 | 5.03 | 7.10 | 5.18 |
| 2 | Saturday, 4 July 2020 | 93.4 | 50.8 | 13 | 8.97 | 6.68 | 10.59 | 12.37 | 10.59 |
| 3 | Monday, 6 July 2020 | 95.9 | 21.6 | 21 | 5.62 | 2.41 | 4.84 | 5.97 | 5.62 |
| 4 | Monday, 6 July 2020 | 20.4 | 21.6 | 4 | 24.78 | 22.89 | 22.70 | 30.85 | 24.78 |
| 5 | Tuesday, 7 July 2020 | 30.6 | 43.0 | 5 | 23.53 | 5.72 | 11.06 | 25.75 | 23.53 |
| 6 | Tuesday, 7 July 2020 | 132.7 | 43.0 | 20 | 1.13 | 1.65 | 1.65 | 2.06 | 1.65 |
| 7 | Wednesday, 8 July 2020 | 87.9 | 42.0 | 14 | 23.59 | 6.40 | 10.84 | 24.82 | 23.59 |
| 8 | Wednesday, 8 July 2020 | 74.7 | 42.0 | 12 | 10.83 | 7.60 | 10.51 | 12.97 | 10.83 |
| 9 | Thursday, 9 July 2020 | 95.9 | 35.2 | 16 | 24.42 | 24.62 | 21.67 | 27.77 | 24.62 |
| 11 | Saturday, 11 July 2020 | 92.9 | 43.4 | 14 | 6.73 | 3.18 | 5.67 | 6.95 | 6.73 |
| 12 | Saturday, 11 July 2020 | 85.9 | 49.0 | 12 | 27.21 | 7.60 | 16.27 | 27.66 | 27.21 |

Table 4. Rock Properties Data

| Lithology | $\rho$ (kg/m3) | $\sigma_{cm}$ (MPa) | $E_{rm}$ (MPa) | $v_m$ | $c_m$ (MPa) | $\Phi_m$ (°) |
|---|---|---|---|---|---|---|
| Slightly weathered and/or fresh andesite | 2600 | 13.00 | 2010 | 0.29 | 1.60 | 40 |

Table 5. Peak Particle Accelaration (PPA) Data

| Transversal (g) | Vertical (g) | Longitudinal (g) |
|---|---|---|
| 0.374 | 0.684 | 0.529 |

### 2.7 Representation of Discontinuities

The influence of geological discontinuities on slope stability was evaluated by comparing an equivalent jointless rock-mass model with an otherwise identical model containing the representative discontinuity set derived from field mapping. A total of 288 discontinuities were measured along the mapped rock exposure. The discontinuity survey recorded strike, dip, persistence, termination, aperture, infilling characteristics, surface roughness, surface shape, Joint Roughness Coefficient (JRC), groundwater condition, and spacing. The measured discontinuities exhibit dip angles ranging from approximately 43° to 85°, indicating predominantly moderate- to steeply dipping structures. The measured spacing ranges from approximately 0.03 to 0.39 m, with a mean spacing of approximately 0.16 m.

The joint surfaces were predominantly characterized by a JRC of 15, representing the majority of the measured discontinuities, while JRC values of 10 and 20 occurred less frequently. The measured strike and dip data were used to identify the dominant structural orientations and to determine the discontinuity set most relevant to the stability of the analyzed slope. Because the numerical analysis was performed in two dimensions, the representative discontinuity incorporated into the RS2 model was selected based on its orientation relative to the analyzed slope cross-section, its persistence, and its potential to provide a preferential shear or deformation path.

Table 6. Joint properties used in the numerical model.

| JCS (MPa) | JRC | Kn (MPa/m) | Ks (MPa/m) |
|---|---|---|---|
| 13 | 15 | 1,600,885 | 160,088 |

The mechanical properties assigned to the explicit joint interfaces are summarized in Table 6. A Joint Compressive Strength (JCS) of 13 MPa and a representative JRC of 15 were adopted for the modeled discontinuity. The normal and shear stiffnesses were calculated as approximately Kn=1.60×106 MPa/m and Ks=1.60×105 MPa/m, respectively. These parameters were assigned to explicit discontinuity interfaces using a frictional slip criterion in RS2, allowing shear displacement and deformation to localize along the modeled joint where its orientation is compatible with the slope geometry.

To quantify the influence of discontinuities under different hydro-mechanical and blasting conditions, the same four stability scenarios were analyzed for both the jointless and jointed models: (1) dry-static, (2) saturated-static, (3) dry-dynamic, and (4) saturated-dynamic. Thus, a total of eight numerical cases were evaluated. The jointless and jointed models retained identical slope geometry, rock-mass properties, mesh configuration, boundary conditions, groundwater assumptions, and dynamic-loading conditions; the presence or absence of the explicit joint interface was the principal structural variable distinguishing the two model configurations. Consequently, the difference in FoS between corresponding jointless and jointed scenarios was used to quantify the incremental contribution of the mapped discontinuity structure to slope instability.

In addition to the FoS comparison, the spatial distribution of deformation and the geometry of the critical failure mechanism were examined to evaluate whether the introduction of the discontinuity altered the predicted failure mechanism. In particular, the analysis was designed to determine whether the failure mechanism remained predominantly rock-mass controlled or became increasingly structurally controlled, with deformation localizing preferentially along the modeled joint plane. This comparison was performed for both dry and saturated conditions and under static and blasting-induced pseudo-static loading, allowing the interaction among joint structure, groundwater saturation, and blasting vibration to be evaluated systematically.

The complete strike–dip dataset was further used to evaluate the dominant joint orientations. A stereographic projection of the measured discontinuities together with the orientation of the analyzed slope face is used to establish the geometric relationship between the mapped joint sets and the slope and to support the selection of the representative discontinuity incorporated into the numerical model.

## 3. Results and Discussion

### 3.1 Factor of Safety of the Quarry Slope

Table 7 summarizes the FoS and PoF results for all eight combinations of groundwater, dynamic loading, and joint representation. Figures 5 and 6 show the corresponding numerical results for the jointless and jointed models, respectively.

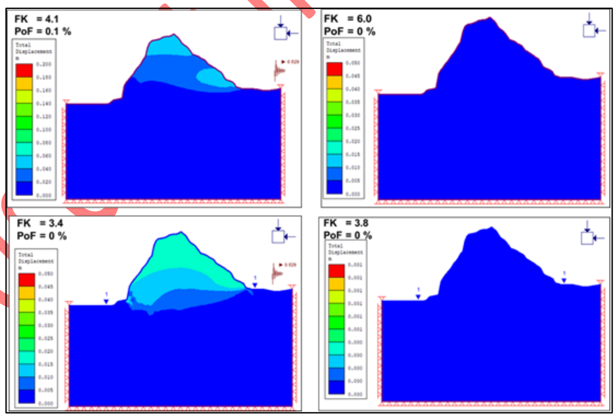


Fig. 5. Results of slope modeling without joints.

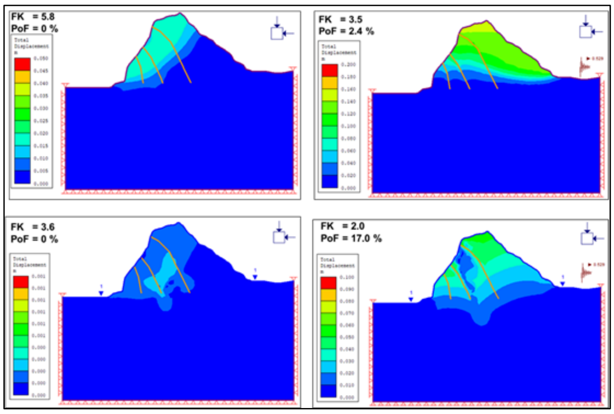


Fig. 6. Results of slope modeling with joints

For the jointless model, the dry-static and saturated-static FoS values are 6.0 and 3.8, respectively. Introducing blast loading decreases FoS to 4.1 under dry conditions and 3.4 under saturated conditions. The model therefore remains above conventional deterministic FoS thresholds, but the reduction demonstrates a measurable dynamic effect even before explicit discontinuities are introduced. Because FoS acceptance criteria depend on project consequence and design stage, the revised manuscript does not treat a single generic threshold as a universal safety criterion.

These results indicate a high deterministic stability margin for the equivalent jointless rock-mass representation under the modeled loading conditions; however, this representation does not capture localized shear resistance along mapped discontinuities.

Introducing the mapped joint set produces only modest reductions under static loading: 3% in the dry case (FoS 6.0 to 5.8) and 6% in the saturated case (FoS 3.8 to 3.6). Under dynamic loading, the joint effect becomes substantially larger: FoS decreases by 15% in the dry case (4.1 to 3.5; PoF 2.9%) and by 42% in the saturated case (3.4 to 2.0; PoF 17%). The saturated-dynamic-jointed scenario is therefore the critical modeled condition.

### 3.2 Combined Effect of Joints, Saturation, and Vibration

The principal finding is the nonlinear interaction between discontinuities, groundwater, and blast loading. Saturation increases pore-water pressure and reduces the effective normal stress acting along the joint plane; consequently, the frictional component of shear resistance decreases. When blast-induced acceleration is superimposed on this weakened interface, stress redistribution can mobilize the discontinuity more readily than under dry conditions. This mechanism explains why the joint-related FoS reduction increases from approximately 15% under dry-dynamic conditions to 42% under saturated-dynamic conditions, rather than representing a simple additive response (Barton and Choubey, 1977).

The change in failure mechanism is also important. In the jointless model, deformation is primarily governed by the equivalent rock-mass strength, whereas the explicit joint interface provides a preferential shear path. Where the selected joint orientation is adverse to the slope face, the critical deformation tends to localize along the discontinuity. This behavior indicates a transition from a predominantly rock-mass-controlled response toward a more structurally controlled deformation mechanism. The finding is consistent with recent numerical studies showing that joint persistence and orientation can significantly modify the failure mechanism of rock slopes.

To translate these numerical findings into an operational blasting criterion, a charge-per-delay sensitivity analysis was performed at the minimum analyzed blast-source-to-slope distance of 25 m. Five charge-per-delay scenarios of 10, 20, 30, 40, and 50 kg/delay were evaluated. Increasing the charge reduced the scaled distance from 7.91 to 3.54 m/kg1/2 and systematically increased the predicted longitudinal PPA from 0.300g to 0.782g. This increase in blast-induced acceleration was accompanied by a progressive reduction in slope stability Table 8.

Table 7. Comparison of slope safety factor (FoS) results

| Condition | Static | | | | | Dynamic | | | | |
|---|---|---|---|---|---|---|---|---|---|---|
| | No Joint | | Joint | | Reduction | No Joint | | Joint | | Reduction |
| | FoS | PoF (%) | FoS | PoF (%) | | FoS | PoF (%) | FoS | PoF (%) | |
| Dry | 6.0 | 0 | 5.8 | 0 | −3% | 4.1 | 0 | 3.5 | 2.9 | −15% |
| Saturated | 3.8 | 0 | 3.6 | 0.1 | −6% | 3.4 | 0 | 2.0 | 17.0 | −42% |

Table 8. Sensitivity of slope stability to explosive charge per delay at a source-to-slope distance of 25 m.

| Q (kg/delay) | SD ($m/kg^{1/2}$) | PPA Trans. (g) | PPA Vert. (g) | PPA Long. (g) | Dry Dynamic FoS | Dry PoF (%) | Saturated Dynamic FoS | Saturated PoF (%) |
|---|---|---|---|---|---|---|---|---|
| 10 | 7.91 | 0.186 | 0.311 | 0.300 | 2.29 | 19.5 | 1.77 | 27.7 |
| 20 | 5.59 | 0.270 | 0.460 | 0.453 | 1.54 | 19.3 | 1.25 | 14.8 |
| 30 | 4.56 | 0.336 | 0.579 | 0.585 | 1.30 | 17.3 | 0.97 | 54.8 |
| 40 | 3.95 | 0.392 | 0.681 | 0.685 | 1.06 | 24.1 | 0.79 | 72.3 |
| 50 | 3.54 | 0.442 | 0.773 | 0.782 | 0.86 | 65.3 | 0.69 | 88.7 |

Under the dry dynamic condition, the calculated FoS decreased from 2.29 at 10 kg/delay to 1.54 at 20 kg/delay, 1.30 at 30 kg/delay, 1.06 at 40 kg/delay, and 0.86 at 50 kg/delay. Thus, 30 kg/delay was selected as the maximum site-specific charge for the dry condition, because it represents the highest investigated charge that still satisfies the adopted FoS acceptance criterion. Increasing the charge to 40 kg/delay increased the predicted longitudinal PPA from 0.585g to 0.685g and reduced the FoS to 1.06, below the adopted stability requirement.

The saturated slope exhibited a substantially lower stability margin. The dynamic FoS decreased from 1.77 at 10 kg/delay to 1.25 at 20 kg/delay, 0.97 at 30 kg/delay, 0.79 at 40 kg/delay, and 0.69 at 50 kg/delay. Because the 30 kg/delay scenario resulted in FoS < 1.0, the maximum charge was reduced to 20 kg/delay under saturated conditions, for which the calculated FoS remained 1.25. These results demonstrate that the allowable explosive charge is strongly dependent on groundwater conditions and that a charge acceptable for a dry slope cannot necessarily be considered acceptable when the jointed rock mass becomes saturated.

The sensitivity analysis therefore supports site-specific maximum charge-per-delay values of 30 kg/delay for dry conditions and 20 kg/delay for saturated conditions at a source-to-slope distance of 25 m. These values should not be interpreted as universal blasting limits because they are conditional on the slope geometry, rock-mass and discontinuity properties, groundwater assumptions, vibration-prediction relationship, and numerical modeling conditions adopted in this study. Moreover, the 11-event PPV regression exhibits considerable scatter (R2=0.376), indicating uncertainty in deterministic vibration prediction. Accordingly, the recommended charge limits should be implemented together with controlled trial blasts and simultaneous monitoring of PPV/PPA, groundwater conditions, and slope displacement.

### 4. Conclusion

This study demonstrates that quarry-slope stability adjacent to tunnel blasting is governed by the combined effects of geological discontinuities, groundwater conditions, and blast-induced vibration. The comparative RS2 analyses show that the explicit representation of the mapped joint structure has a relatively limited effect under static conditions, reducing the FoS by approximately 3% under dry conditions and 6% under saturated conditions. Under dynamic loading, however, the influence of the discontinuity becomes substantially greater, with FoS reductions of approximately 15% under dry conditions and 42% under saturated conditions relative to the corresponding jointless models. The saturated-dynamic-jointed condition, with an FoS of 2.0 and PoF of 17%, represents the most critical condition among the eight baseline scenarios evaluated.

The numerical results further indicate that groundwater saturation amplifies the destabilizing effect of blasting by reducing the available shear resistance along discontinuities, thereby promoting a transition from predominantly rock-mass-controlled deformation toward a more structurally controlled response. This finding emphasizes that blasting effects on jointed rock slopes cannot be evaluated solely from vibration amplitude without considering groundwater and discontinuity conditions.

The charge-per-delay sensitivity analysis at a 25 m blast-source-to-slope distance provides an operational basis for controlling blasting as tunnel excavation approaches the quarry slope. Increasing the explosive charge from 10 to 50 kg/delay increased the predicted longitudinal PPA from 0.300g to 0.782g and progressively reduced slope stability. Based on the adopted stability criteria, the analysis supports a maximum site-specific charge of 30 kg/delay under dry conditions, corresponding to a dynamic FoS of 1.30, whereas under saturated conditions the recommended maximum charge is reduced to 20 kg/delay, corresponding to a dynamic FoS of 1.25. At 30 kg/delay under saturated conditions, the FoS decreases to 0.97, indicating an unacceptable stability condition in the modeled scenario.

These charge limits are site-specific rather than universal design values, as they depend on the investigated slope geometry, rock-mass and joint properties, groundwater conditions, blast-source distance, and vibration-prediction model. Given the scatter in the site PPV regression (R2=0.376), the recommended limits should be verified through controlled trial blasts accompanied by simultaneous monitoring of PPV/PPA, groundwater conditions, and slope displacement. The results therefore support an adaptive blasting strategy in which allowable charge per delay is reduced when saturated slope conditions are encountered.

## 5. Recommendation

Based on the numerical and sensitivity analyses, blasting near the quarry slope should be controlled according to groundwater conditions and the blast-source-to-slope distance. At the minimum analyzed distance of 25 m, the recommended maximum charge per delay is 30 kg under dry conditions and should be reduced to 20 kg under saturated conditions. These values are site-specific and should not be directly extrapolated to shorter distances or substantially different geological, hydrogeological, or slope conditions. The proposed charge limits should be verified through controlled trial blasts accompanied by monitoring of PPV/PPA, groundwater conditions, and slope displacement. Particular attention should be given during periods of high groundwater or prolonged rainfall because saturation significantly increases the destabilizing effects of discontinuities and blasting vibration. Periodic geotechnical inspection of critical joint zones and continuous evaluation of blasting performance are also recommended, with the numerical model and site-specific vibration relationship updated as additional monitoring data become available.

## Acknowledgements

The authors would like to thank the Mining Engineering Department, Universitas Negeri Padang and the Mining Engineering Study Program, Institut Teknologi Bandung for their support during this research, as well as PT. Kereta Cepat Indonesia Cina (KCIC) and the quarry operators around Tunnel 4 for granting access to the field data used in this study.

## References

Aditya, F. et al. (2025) 'Mine Slope Stability Analysis CV . Putra Idola Against the Padang-Painan Cross Road with GSI Method and Rock Mass Rating', pp. 129–144.

Al-E'Bayat, M. et al. (2024) 'Numerical Investigation for the Effect of Joint Persistence on Rock Slope Stability Using a Lattice Spring-Based Synthetic Rock Mass Model', Sustainability, 16(2), p. 894. doi: 10.3390/su16020894.

Azizi, M. A. (2018) 'Three dimensional slope stability analysis of open pit limestone mine in Rembang District', in. Central Java: IOP Conference Series: Earth and Environmental Science.

Barton and Choubey (1977) 'The shear strength of rock joints. Rock Mechanics.pdf'.

Barton, N. R. (1972) 'A model study of rock-joint deformation', International Journal of Rock Mechanics and Mining Sciences and, 9(5), pp. 579–582. doi: 10.1016/0148-9062(72)90010-1.

Devy, S. D. and Hutahayan, P. P. (2021) 'Engineering , Environment , and Technology Groundwater Effect on Slope Stability in Open Pit Mining : a Case of West Kutai Regency, East Kalimantan, Indonesia', 6(4). doi: 10.25299/jgeet.2021.6.4.6226.

Dowding, C. H. (1985) Blast Vibration Monitoring and Control. Englewood Cliffs: Prentice Hall.

Du, S.-G. et al. (2022) 'A new approach for evaluation of slope stability in large open-pit mines: a case study at the Dexing Copper Mine, China', Environmental Earth Sciences, 81(3), p. 102. doi: 10.1007/s12665-022-10223-0.

Gofar, N. and Rahardjo, H. (2017) 'Saturated and unsaturated stability analysis of slope subjected to rainfall infiltration', MATEC Web of Conferences. Edited by I. Iskandar et al., 101, p. 05004. doi: 10.1051/matecconf/201710105004.

Heriyadi, B. et al. (2026) 'GEOTECHNICAL STABILITY AND ENVIRONMENTAL RISK', 30(141), pp. 56–66.

Irwandy Arif (2016) Geoteknik Tambang. 1st editio. Edited by A. L. dan Suprianto. Jakarta: PT Gramedia Pustaka Utama.

Jiang F., Xiong, Y., Han, R., & X. Y. (2014) 'Analysis of Instability and Controlling Measurements for Super-Large Cross Section of High Speed Railway Tunnel Portal'. doi: 10.3969/j.issn.1006-4540.2013.06.006.

Lee, W.-S. et al. (2013) 'Determination of Optimized Blasting Pressure through Critical Volumetric Strain Monitoring', Journal of korean society of hazard mitigation, 13(4), pp. 191–197. doi: 10.9798/KOSHAM.2013.13.4.191.

Luo, S. et al. (2023) 'Dynamic Response and Safety Evaluation for the Adjacent Viaduct Under the Influence of Subway Connecting Passage Blasting', Indian Geotechnical Journal, 53(2), pp. 362–376. doi: 10.1007/s40098-022-00682-4.

Ma, C. et al. (2025) 'Radar Monitoring and Numerical Simulation Reveal the Impact of Underground Blasting Disturbance on Slope Stability', Remote Sensing, 17(15), p. 2649. doi: 10.3390/rs17152649.

Ma, Z. et al. (2021) 'Slope Stability Analysis under Complex Stress State with Saturated and Unsaturated Seepage Flow', Geofluids. Edited by G. Zhang, 2021, pp. 1–11. doi: 10.1155/2021/6637098.

Al Mandalawi, M. (2024) 'The Influence of Rock Slope Scales of Joint Network and Slope Height on the Stability and Failure Mechanisms', IRAQI BULLETIN OF GEOLOGY AND MINING, 20(1), pp. 139–149. doi: 10.59150/ibgm2001a09.

Prassetyo, S. H. et al. (2024) 'Evaluation of Blast-Induced

Ground Vibration in Urban Area for the Jakarta-Bandung HSR Tunnel #11', Geotechnical and Geological Engineering, 42(8), pp. 7255–7285. doi: 10.1007/s10706-024-02926-x.
Putra, K. E. et al. (2026) 'Engineering , Environment , and Technology Optimization of Bench Width and Vertical Bench Position for Claystone Slopes Using the Limit Equilibrium Method under a Safety Factor Constraint', 11(2). doi: 10.25299/jgeet.2026.11.02.28001.
Sun, P. and Li, R. (2023) 'Dynamic response of high and thin rock slope under blasting vibration: a case study', Journal of Vibroengineering, 25(6), pp. 1181–1197. doi: 10.21595/jve.2023.23195.
Sun, Z. et al. (2024) 'Numerical Analysis of Slope Stability in Open Pit Mining Based on an Integrated Geology and Geomechanics Approach', in 58th U.S. Rock Mechanics/Geomechanics Symposium. ARMA. doi: 10.56952/ARMA-2024-0499.
Wang, H. et al. (2023) 'Safety Evaluation and Application of Blasting Vibration Based on an Improved Hilbert–Huang Transform', Rock Mechanics and Rock Engineering, 56(6), pp. 3971–3991. doi: 10.1007/s00603-023-03272-9.
Wong, H. N. dan Pang, P. L. R. (1992) Assessment of Stability of Slopes Subjected to Blasting Vibration. Hongkong: Geotechnical Engineering Office.
Xiong, Q. et al. (2021) 'Study on slope stability during tunnel construction in water rich soft soil area', IOP Conference Series: Earth and Environmental Science, 783(1), p. 012001. doi: 10.1088/1755-1315/783/1/012001.
Zvarivadza, T. et al. (2025) 'Deep learning-powered rock mass classification: Predicting RMR from Q-system parameters with high accuracy', Rock Mechanics Bulletin, 4(4), p. 100219. doi: 10.1016/j.rockmb.2025.100219.